Magic carpet breakup of a drop impacting onto a heated surface in a depressurized environment

Ryuta Hatakenaka [a,b,c,*], Jan Breitenbach [b], Ilia V. Roisman [b], Cameron Tropea [b], Yoshiyuki Tagawa [c]

[a] Japan Aerospace Exploration Agency, Research and Development Directorate, 2-1-1 Sengen, Tsukuba, Ibaraki 305-8505, Japan
[b] Technische Universität Darmstadt, Institute of Fluid Mechanics and Aerodynamic, Alarich-Weiss-Straße 10, 64287 Darmstadt, Germany
[c] Tokyo University of Agriculture and Technology, Institute of Global Innovation Research, 2-24-16 Nakamachi, Koganei, Tokyo 184-8588, Japan

ABSTRACT

Drop impact onto a hot substrate leads to various hydrodynamic outcomes depending on the substrate temperature and the impact parameters: deposition, drop dancing, thermal atomization, and finally rebound at temperatures above the dynamic Leidenfrost condition. In the present experimental study this parameter space has been extended to conditions of a depressurized environment (1–101 kPa), which are relevant to space applications such as a reentry spaceship or a rocket engine. The impact onto a superheated smooth substrate with relatively small impact velocities (0.1–0.46 m/s) has been captured using a high-speed video camera system. Under these conditions two new modes of drop outcome have been identified; *magic carpet breakup*, in which the drop splashes immediately after the impact, leading to extensively large lateral deformation and upward drop movement, and *tiptoeing*, in which the drop bounces back with a time scale similar to *capillary rebound* (so-called *rebound*) accompanied by a significant fluctuation of the outer shape and secondary droplet generation triggered by successive attach-and-detach cycles. These new modes occur at a temperature range between the *deposition* regime and the *capillary rebound* regime. Detailed regime maps indicating the type of drop outcome for different pressures and substrate temperatures have been constructed. Moreover, a hypothesis on the mechanism of *magic carpet breakup* is presented and a theoretical model, in which a classical bubble growth model for pool boiling is extended to bubble growth in a drop and correlated with drop kinematics, is developed. The numerical solution is in good qualitative agreement with the experimental data for the bubble burst time and for the change in drop velocity.

© 2019 The Authors. Published by Elsevier Ltd. This is an open access article under the CC BY-NC-ND license (http://creativecommons.org/licenses/by-nc-nd/4.0/).

1. Introduction

Impingement of a spray onto a heated wall can be observed in many industrial applications such as spray cooling, gas turbines or in internal combustion engines [1,2]. In a rocket engine that operates under a much wider range of pressure and temperature, cryogenic propellant and oxidizer are sprayed onto the walls of the combustion chamber to prevent it from overheating [3]. It is well known that heat flux becomes larger as the wall temperature increases, however, it drastically decreases when exceeding a threshold called critical heat flux, until it reaches its minimum value at the Leidenfrost point [4–6]. The so-called Leidenfrost temperature is the threshold between *transition boiling* and *film boiling*. This drastic reduction in cooling efficiency could be a serious

problem in many technological processes where very hot surfaces have to be cooled quickly, for example in metallurgical or metal working processes such as quenching [7,8] or during cooling of solar panels [9,10].

Comprehensive reviews of spray cooling phenomena can be found in Liang and Mudawar [11,12] and Breitenbach et al. [13]. Although interaction of a spray with a hot wall has been widely investigated over the past decades [14–19], the underlying physics of the involved phenomena are not yet fully understood. The current design of spray cooling systems thus remains mainly empirical. An empirical approach is not always desirable since it requires additional testing, leading to increased costs, especially when the device utilizes special fluids or operates under extreme conditions.

The interaction of a single drop with a hot substrate under atmospheric pressure has been extensively investigated, leading to comprehensive reviews of this phenomenon by Breitenbach et al. [20], Liang and Mudawar [20], Yarin et al. [21]. The influence of various parameters, e.g. impact parameters, fluid properties,

* Corresponding author at: Japan Aerospace Exploration Agency, Research and Development Directorate, 2-1-1 Sengen, Tsukuba, Ibaraki 305-8505, Japan.
E-mail address: hatakenaka.ryuta@jaxa.jp (R. Hatakenaka).

Nomenclature

α_l	thermal diffusivity of liquid
A	bubble growth rate
A_1	bubble growth rate in horizontal direction
A_2	bubble growth rate in vertical direction
c_{pv}	specific heat of vapor
c_{pl}	specific heat of liquid
D_0	initial drop diameter
D_{max}	maximum drop diameter
e_w	thermal effusivity of substrate
e_l	thermal effusivity of liquid
$E_{kin,l}$	total kinetic energy of liquid
ϵ	radius ratio R_b/R_{lim}
ϵ_1	radius ratio in horizontal direction
ϵ_2	radius ratio in vertical direction
F_v	upward force applied by growing bubble
Ja	Jakob number
L	specific latent heat
m_{drop}	total mass of drop
p_0	atmospheric pressure
p_{NCG}	pressure of non-condensable gas in a bubble
p_{ch}	chamber pressure
p_l	pressure of surrounding liquid
p_{req}	saturated vapor pressure at T_{req}
p_{sat}	saturation pressure
p_v	pressure of vapor in a bubble
q_1	heat flux through thermal boundary layer in the substrate
q_2	heat flux due to evaporation
r_c	cavity radius
ρ_v	density of vapor
ρ_{v0}	density of vapor under atmospheric condition
ρ_l	density of liquid
r	radial position in the drop
R_0	initial drop radius
R_{cont}	contact radius
R_b	bubble radius
R_{b1}	bubble radius in horizontal direction
R_{b2}	bubble radius in vertical direction
R_{bb}	bubble burst radius
R_{lim}	radial dimension for the end of integration
$\mathcal{R}_{H_2O}$	gas constant of water
σ	surface tension
t	time
t_{bb}	bubble burst time
t_{gr}	bubble growing time
t_w	waiting time for activation
T_0	substrate temperature
T_l	initial drop temperature
T_{cont}	contact temperature between drop and substrate
T_{req}	required temperature for activation
T_{sat}	saturation temperature
T_L	Leidenfrost temperature
ΔT_{req}	required superheating temperature
τ	dimensionless time
τ_{bb}	dimensionless bubble burst time
τ_{gr}	dimensionless bubble growing time
τ_w	dimensionless waiting time
u_r	radial velocity of liquid
U_0	drop impact velocity
U_1	drop velocity after detachment
V	volume of bubble
v_v	specific volume of vapor
v_l	specific volume of liquid
W	work done by a growing bubble to the surrounding liquid

substrate material and substrate roughness on the Leidenfrost temperature T_L have been extensively studied. Many empirical correlations have been proposed by numerous researchers [20,22]. Bernardin and Mudawar [23] proposed a model for sessile drops based on classical bubble growth theory. It was extended to impinging drops by taking into account the change in fluid properties due to a rise in pressure resulting from drop impact at the liquid-solid interface [24]. Aursand et al. [25] studied the interfacial stability of film boiling and concluded that the vapor film collapses depending on a balance between thermocapillary instabilities and vapor thrust stabilization. This finally yields a prediction of T_L consistent with experimental data found in literature for various liquids.

The influence of surrounding gas on the drop impact has attracted much attention since Xu et al. [26] published their pioneering work in which the suppression of splash triggered by depressurized environment was observed. Mandre et al. [27] and Mani et al. [28] have theoretically and numerically explained the mechanism of how environmental pressure affects dimple formation at the liquid-air interface. Driscoll et al. [29] conducted further experiments and showed that the time period for thin liquid sheet ejection for various sets of parameters (e.g., impact velocity, gas pressure, gas molecular weight, liquid viscosity, liquid surface tension) may collapse onto a single curve as a function of the molecular weight and surrounding gas pressure along with liquid viscosity and drop impact velocity. They also presented that a ring of microbubbles is entrained in a depressurized environment, in addition to the central bubble that is always entrained regardless of the surrounding pressure. Interestingly, according to their

report, the bubble entrainment at the rim of the lamella is influenced not by the surrounding pressure or impact velocity but by the rim spreading velocity. The thickness distribution of the entrained gas layer and its time evolution have been characterized by means of high speed interferometry measurement [30–35]. It is noteworthy that nucleation of contact between a liquid and solid occurs from a surprisingly large distance of more than 200 nm [31,33]. The height is only a few times the mean free path in the gas at the surrounding pressure, which suggests that a rarefied gas effect may play an important role in promoting collapse of the gas layer. Li et al. [36] recently measured the radius and thickness of the entrained air layer under depressurized environment and proposed a new scaling law that takes a rarefied gas effect into account.

Drop impact onto a heated surface under variable pressure involves more complicated physics. The influence of the surrounding gas on the air cushion effect, i.e. the lift force due to the compression of surrounding gas between the drop and substrate, should also play an important role. Furthermore, the changes in fluid properties (e.g. saturation temperature, vapor density) and the condition for the onset of boiling change due to the change of surrounding pressure and should be taken into account. Despite the complexity of the problem there is insufficient experimental data under different pressure conditions, thus the phenomena are poorly understood. Celestini et al. [37] evaluated the lifetime of a static Leidenfrost drop on a heated surface. Orejon et al. [38] identified the static T_L for a water drop in a depressurized environment and proposed an empirical model that correlates with the Clausius-Clapeyron equation, whose applicability to ethanol has

been confirmed by Limbeek et al. [39]. The influence of the surrounding pressure on the dynamic T_L have been studied by Buchmüller [40] for elevated pressures and by van Limbeek et al. [39] for a depressurized environment. Breitenbach et al. [41] proposed a theoretical model of heat transfer during drop impact in the nucleate boiling regime to estimate the lifetime of an impinging drop and demonstrated its good agreement with literature results, including elevated pressure conditions given in [40]. Basically, static and dynamic T_L seem to follow the trend of a given fluid's saturation temperature under both elevated and reduced pressure, although dynamic T_L stops decreasing and then begins to increase for the case of an extreme decrease in surrounding pressure [39]. However, a pure physics based model for the dynamic T_L under elevated or reduced pressure has not yet been developed. Further understanding of the interfacial phenomenon among the drop, substrate, surrounding gas, and generated vapor, especially in the initial phase of drop impact, is necessary in order to establish a physical model to estimate drop behavior and finally spray cooling performance under variable surrounding pressure conditions.

The present experimental and theoretical study aims to provide a more complete picture of a single drop impact onto a heated surface in a depressurized environment that contributes to prediction of the heat removal characteristic of spray cooling under these conditions. The present study is motivated by space technology applications. A spray cooling device for internal equipment of a re-entry vehicle such as the Space Shuttle operates over a wide range of environmental pressure from high vacuum to atmospheric pressure accompanied by variable gravity [42]. In this application, minimization of the coolant mass that is exhausted to the outside without vaporization is necessary to benefit from the large latent heat of vaporization per mass. Furthermore, operation of the spray cooling device at larger heat flux leads to mass reduction of the evaporator. In a rocket engine, the liquid propellant and oxidizer are sprayed onto the internal wall of the combustion chamber to maintain the maximum temperature below the material limit. An intermittent thrust of rocket engine is highly in-demand for space exploration missions in the future, in which reliable prediction of spray cooling as well as combustion are critical issues.

In this contribution a single drop impact, its spreading, breakup, rebound and other phenomena are observed using a high-speed video system. First the experimental method is described in Section 2, and then two regime maps for two different impact velocities (0.1 m/s and 0.46 m/s) under a wide range of depressurized conditions (1–101 kPa) are presented in Section 3. Here, two new modes of drop outcome have been identified; *magic carpet breakup*, in which the drop splashes immediately after the impact, leading to extensively large lateral deformation and upward drop movement, and *tiptoeing*, in which the drop bounces back with a time scale similar to *capillary rebound*, accompanied by a significant fluctuation of outer shape and secondary droplet generation triggered by successive attach-and-detach cycles. The kinematics of these two outcomes are presented in Section 4.

The experimental results, the physical hypotheses, explaining the appearance of the magic carpet phenomena, and some preliminary modeling approaches have been previously published in the pioneering study [43]. Yu et al. [44] recently reported a similar phenomenon, which is called "explosive bouncing" in their report, including a total internal reflection (TIR) imaging result of a growing bubble between the drop and substrate. We have also observed *magic carpet breakup* under atmospheric conditions in a separate experiment, in which the drop impacts onto a heated sand-blasted aluminum surface and the substrate temperature lies within a certain, narrow range (Fig. 1). Similar explosive drop
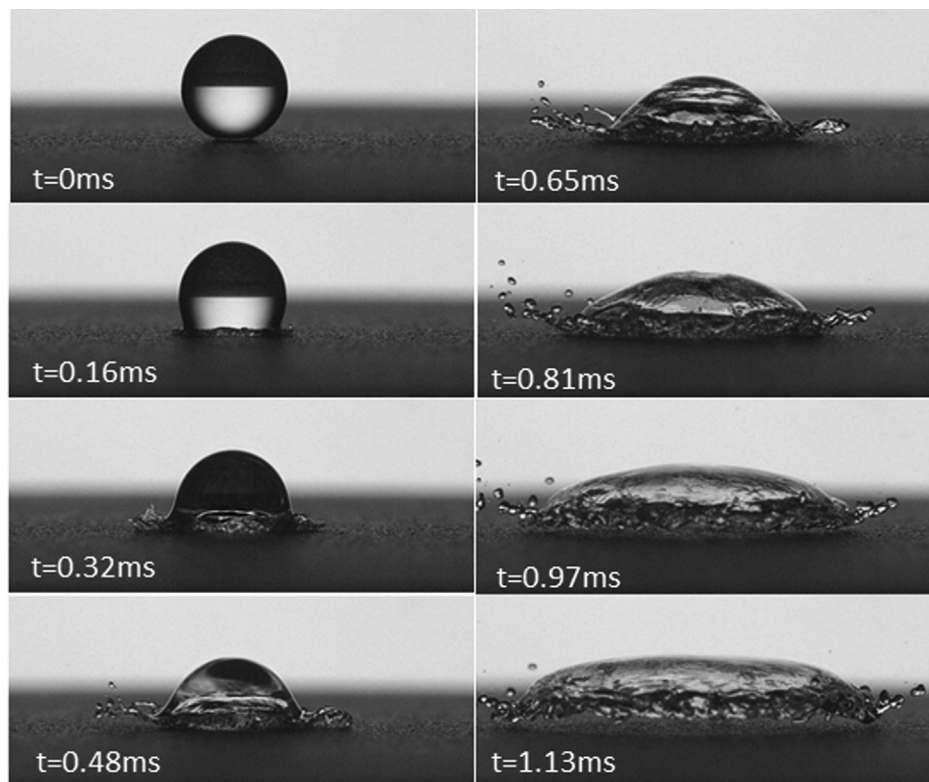

Fig. 1. Time sequences of *magic carpet breakup* observed by the authors under atmospheric conditions in a separate experiment. The surface material is sandblasted aluminium, whose root-mean-square surface roughness is approximately 4 μm, measured using atomic force microscopy. The conditions are $T_0 = 170\,°C, p_{ch} = 101$ kPa, $U_0 = 1.72$ m/s, and $D_0 = 2.2$ mm.

phenomena have also been observed under atmospheric conditions for a water drop impacting onto a heated titanium oxide nanotube surface [45] and heated random silicon nanowires [46], and for a static Leidenfrost drop made of an aqueous solution of surfactant on a smooth heated surface [47]. Nonetheless, the mechanism of these phenomena are not sufficiently understood.

In this study, a hypothesis on the mechanism of *magic carpet breakup* is given in Section 5, and then a theoretical model for the activation, growth, and bursting of a bubble between the drop and the substrate based on classical bubble growth theory is developed in Section 6. The theoretical predictions for the bubble burst time and upward drop velocity agree well with the experimental results. An extensive deformation accompanied by upward motion happens in a relatively narrow range, however *Magic carpet breakup* and *tiptoeing*, which are supposed to have a common physical mechanism, are the dominant outcomes under a depressurized environment above the threshold temperature for bubble activation. Understanding of this hydrodynamic behavior is definitely crucial in spray cooling, since the mass efficiency significantly decreases if the sprayed fluid is vented to the exterior environment before vaporization. This result also provides insight into the mechanism of similar explosive drop phenomena.

2. Experimental setup

Fig. 2 shows a sketch of the experimental apparatus, which consists of a pressure control system, a drop generator, a heating system, and a high-speed camera recording system.

A depressurized environment is created with a transparent acrylic vacuum desiccator with dimensions of $260 \times 280 \times 410$ mm and an oil rotary vacuum pump. An electric valve between these components is controlled by a pressure controller (*K3HB, OMRON Co.*) in combination with an absolute pressure transducer (*PAB-A-200KP, Kyowa Electronic Instrument Co.*). The chamber pressure p_{ch} is measured with two different sensors: for the test case above 5 kPa an absolute pressure transducer (*PAB-A-200KP*) is used while for lower cases (2.5 kPa and 1 kPa) a capacitance manometer (*Baratron 627F21TBC2B, MKS Instrument Inc.*) has been applied. The pressure control accuracy is $50 \text{ kPa}^{+0.5}_{-0.0}$, $25 \text{ kPa}^{+0.5}_{-0.0}$, $10 \text{ kPa}^{+0.5}_{-0.0}$, $5 \text{ kPa}^{+0.5}_{-0.0}$, $2.5 \text{ kPa}^{+0.3}_{-0.0}$, and $1.0 \text{ kPa}^{+0.3}_{-0.0}$ respectively.

Stable drop generation is one of the challenges in this experiment due to the degassing of dissolved gas and the boiling of liquid enhanced by the low surrounding pressure. An airtight syringe charged with ultrapure water is connected to a thin dispenser nozzle (*TECDIA Co. Ltd.*) having an outer diameter of 0.2 mm at the tip, which generates a drop with diameter of 1.8–2.2 mm. It is connected to a syringe pump aligned vertically so that the water surface in the syringe is located a few centimeters lower than the outlet of the syringe and both the tube and nozzle are empty as shown in Fig. 2. For preconditioning, the chamber is depressurized to the ultimate pressure (on the order of 100 Pa) and maintained in that state for more than 30 min for degassing of dissolved gas in the water. A gas or water vapor bubble grows very large due to the low pressure. The upward alignment of the syringe as well as the empty state of the tube and nozzle allow the gas or water vapor to evacuate through the tube and nozzle. After the degassing procedure, the syringe pump is operated to move the piston of the syringe upward so that both the syringe and piping are filled with liquid water. The nozzle is manually cooled down by opening the chamber door and spraying volatile fluid when the nozzle temperature exceeds approximately 35 °C, in order to avoid boiling inside the nozzle and maintain almost the same drop temperature to ensure repeatability.

The impact velocity of a drop U_0 is controlled by changing the height of the heating system. In this study, two impact velocities, a very small velocity $U_0 \approx 0.1$ m/s and a moderate velocity $U_0 \approx 0.46$ m/s, are adopted as the test cases. The actual velocity is calculated from the vertical displacement from the first image after the release to the image just before the impact, assuming a free fall.

A silicon wafer with diameter of 50.8 mm, thickness of 0.28 mm, and surface roughness of less than 10 nm (typically less than 5 nm) is used as a heated substrate. It is attached to a stainless-steel heating block with dimensions of $50 \times 50 \times 10$ mm with thermal filler compound. The block is heated using cartridge heaters controlled by a temperature controller with a type-K thermocouple inserted into the block. The temperature of the silicon wafer is directly measured by another type-K thermocouple bonded to its bottom side with heat conductive adhesive.

The behavior of the drop during impact is captured with a high-speed camera (*FASTCAM SA-X, Photron Ltd.*) through the side wall of the chamber with a spatial resolution of 33 μm per pixel. A high power LED backlight is placed onto the opposite side wall with a diffusion plate in order to perform shadowgraphy imaging. The frame rate is set at 5000 frames per second (fps) since the experiment reported in this study was initially aimed towards a general survey of drop outcomes over a wide range of chamber pressures and substrate temperatures. All experimental images are analyzed by using the image processing toolbox of *MathWorks MATLAB*. In
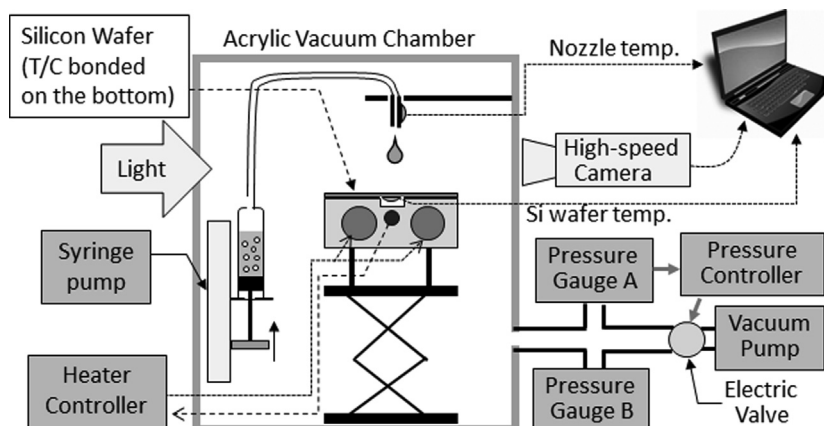

Fig. 2. Sketch of the experimental setup. The piston of the syringe is positioned for the degassing process. The temperature of the heater block is controlled so that the temperature of silicon wafer measured directly at the bottom side is maintained at the target temperature. The chamber pressure is maintained at the target value by controlling the electric valve.

each image the drop diameter D_0 is calculated based on an equivalent diameter of a drop with the same number of pixels within the detected drop. The center of gravity is calculated by averaging the coordinates of all pixels corresponding to the drop in each binarized image. Furthermore, the upward velocity is calculated in-between two successive images from the calculated coordinates and then time-averaged; start time for the time-averaging is the moment when the drop detaches from the surface, whereas the end time is the moment when the binarized drop image disintegrates into multiple pieces, neglecting tiny secondary droplets or when the drop again contacts the surface, whichever occurs first. The maximum drop diameter D_{max} for each test case is determined as the maximum value of the horizontal drop length, which is measured as the difference between the maximum and the minimum x-coordinate.

3. Outcomes of drop impact

The outcomes of drop impact under atmospheric conditions have been extensively investigated in the past [48–50]. Given the relatively small impact velocity, neither an inertia dominated breakup nor thermal atomization [51,52] has been observed for any of the substrate temperature conditions in this study (60−250 °C). Thus, the drop outcomes under atmospheric conditions can be categorized into *deposition* and *rebound* in this study. Although the latter is usually referred to simply as *rebound* in the literature, we term it *capillary rebound* to distinguish it from newly identified outcomes in this study.

Fig. 3 show typical images of the outcomes of drop impact onto a heated substrate with moderate impact velocity ($U_0 = 0.46$ m/s) in a depressurized environment. Additionally, the corresponding videos are added in the supplementary materials [53], where the video number corresponding to each sub-figures are written in the caption of Fig. 3. Two different well-known outcomes, (a) *capillary rebound* and (f) *deposition*, were also observed in a depressurized environment when the substrate temperature is sufficiently high or low. In-between these two outcomes, a new outcome named *vapor rebound*, which is subdivided into *magic carpet breakup* and *tiptoeing*, has been identified under depressurized conditions, as shown in Fig. 3(b)–(d). A transition regime is also observed, as shown in Fig. 3(e). As all of these outcomes are supposed to be triggered by vapor generation due to partial or full contact between liquid and the substrate, we generally refer to these as *vapor rebound*.
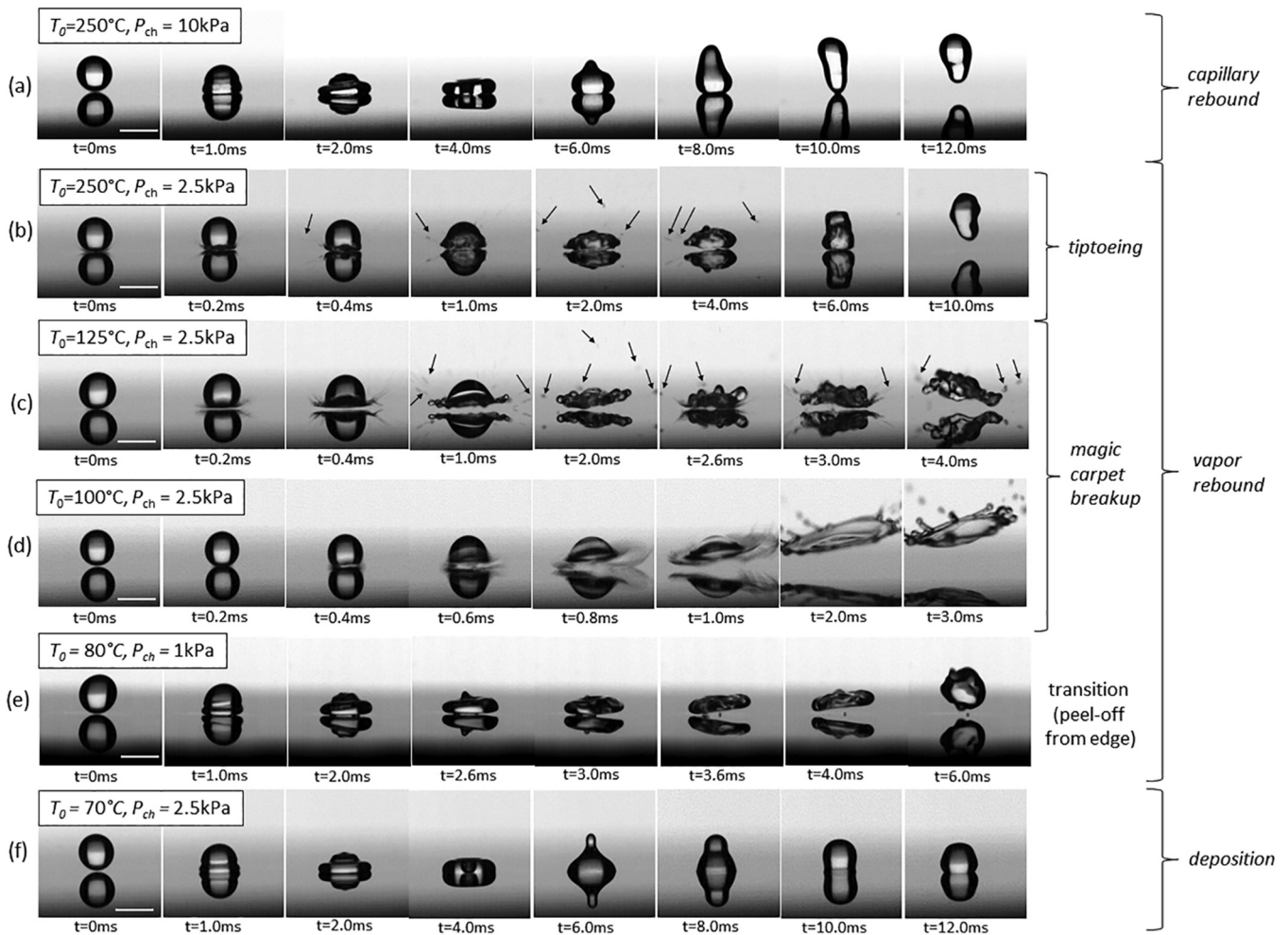

Fig. 3. Drop impact of different observed hydrodynamic outcomes in a depressurized environment: (a) *capillary rebound* (supplemental video 1), (b) *tiptoeing* (supplemental video 2), (c) *magic carpet breakup* (supplemental video 3), (d) *magic carpet breakup* (supplemental video 4), (e) a transition state in which the drop is peeled off from the edge (supplemental video 5) (f) *deposition* (supplemental video 6). The chamber pressure and substrate temperature for each snapshot are given in the image. The impact velocity and drop diameter are similar for all cases ($U_0 = 0.46$ m/s, $D_0 = 2.0$ mm). The largest drop deformation is observed at a slightly higher substrate temperature than the *deposition* regime, and the drop deformation becomes smaller as the substrate temperature increases. The arrows in (b) and (c) indicate some of the secondary droplets observed in the experiments. Note that the time interval is not identical. All of (b), (c), (d) are categorized as *vapor rebound* in Fig. 5. The scale bar shown in the first image is 2.0 mm. The contrast of the images has been enhanced.

As shown in Fig. 3(e), when the substrate temperature T_0 is slightly higher than that for the *deposition* case, a transition regime occurs in which the drop deposits onto the substrate ($t = 1.0$ ms), then the contact region between the drop and substrate decreases ($t = 2.0 - 3.6$ ms), and finally the drop peels off from the substrate ($t = 3.6 - 4.0$ ms). There are some varieties of the drop shape evolution in this regime. Note that the drop outcomes in this paper are categorized based on drop motion rather than boiling state. The boundary between *deposition* and this transition regime is determined based on whether the drop finally detaches from the substrate or not.

By slightly increasing the surface temperature T_0 in Fig. 3(d), the drop first deposits onto the substrate ($t = 0.2$ ms), and then splashes ($t = 0.4 - 0.6$ ms), leading to extensively large lateral deformation and upward drop movement ($t = 1.0 - 3.0$ ms). At relatively high substrate temperature, as shown in Fig. 3(c), an intense but small-scale splash is observed immediately after touching down ($t = 0.2$ ms), resulting in large lateral deformation of the bottom part of the drop, whereas the upper part retains its original shape ($t = 0.4$ ms). In this case, the drop still has a downward velocity even after the first splash, leading to subsequent contact and splash ($t = 2.6$ ms). The drop outcomes shown in Fig. 3(c) and (d) are both named *magic carpet breakup* as the lower part of the drop in (c) deforms into a magic carpet-like shape and hovers temporarily ($t = 0.2 - 2.0$ ms) or the entire drop in (d) moves away from the substrate ($t = 1.0$ ms).

By further increasing the substrate temperature T_0, large deformations and disintegration of the drop vanish. The drop bounces back with a time scale similar to that of *capillary rebound*, being accompanied by a significant fluctuation of the outer shape and secondary droplet generation. The arrows in Fig. 3(b) indicate secondary droplets. In this case, successive partial contact seems to be made between the liquid and substrate according to visual observation. Similar phenomenon is also observed when the impact velocity is very small ($U_0 \approx 0.1$ m/s) as shown in Fig. 4. Here, a successive attach-and-detach cycle of a small part of the drop is clearly observed, leading to significant drop deformation in each cycle. Both of Fig. 3(b) and Fig. 4 are categorized in a new drop outcome named *tiptoeing*.

When substrate temperature T_0 becomes significantly high the outcome changes to *capillary rebound* for $p_{ch} = 10$ kPa, as shown in Fig. 3(a), whereas it remains the same in the *tiptoeing* regime even at the highest temperature $T_0 = 250$ °C ($U_0 = 0.46$ m/s) for lower ambient pressures $p_{ch} = 1 - 5$ kPa. The determination between *tiptoeing* and *capillary rebound* is made based on the existence of observable secondary droplets. This boundary does not necessarily coincide to that of film boiling. Nishio and Hirata [54] investigated the existence of direct contact between the drop and the heated surface with a static Leidenfrost drop via an electrical probe and reported that considerable direct contact exists between the drop and solid substrate even at substrate temperatures of 500 °C. Therefore, tiny-scaled direct contact and intensive evaporation are still considered to occur in the temperature range of *capillary rebound* in our experiments.

Complementary regime maps for two different impact velocities are shown in Fig. 5. Considering the limited thermal
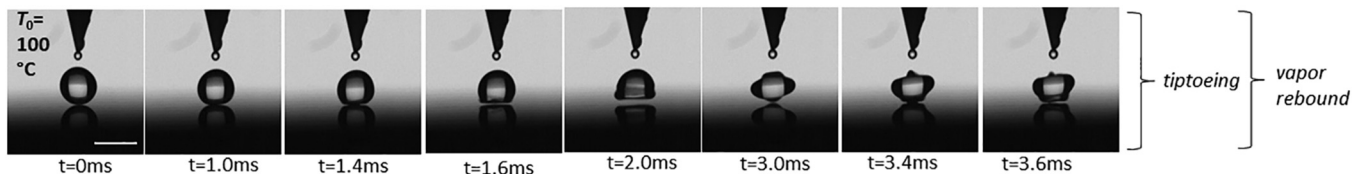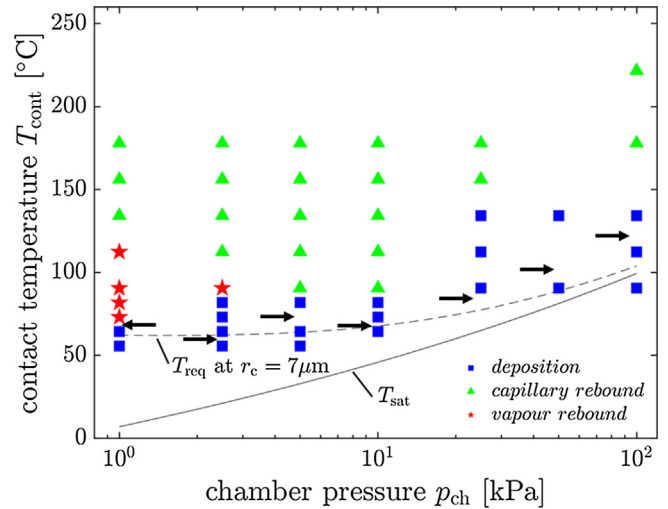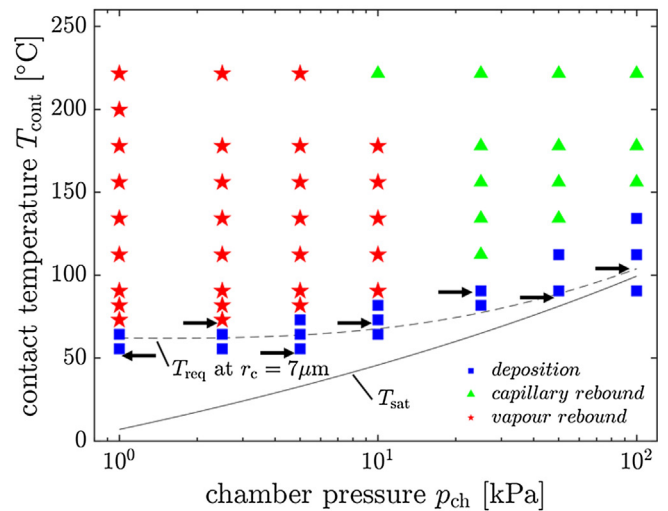
(a)

(b)

Fig. 5. Regime map for (a) very small impact velocity ($U_0 \approx 0.1$ m/s, $D_0 \approx 2.0$ mm) and (b) moderate impact velocity ($U_0 \approx 0.46$ m/s, $D_0 \approx 2.0$ mm). The contact temperature T_{cont} (the vertical axis) is calculated using Eq. (1). The solid curve denotes the saturation temperature (T_{sat}) of water; the dashed curve denotes the required substrate temperature (T_{req}) defined in Eq. (3) as being fitted to the experimental result by setting cavity radius $r_c = 7 \times 10^{-6}$ m. The outcomes are marked as ■ *deposition*, ▲ *capillary rebound*, and ★ *vapor rebound*. Note that *vapor rebound* includes both *magic carpet breakup* and *tiptoeing* as shown in Fig. 3. Thick arrows denote the threshold between *film evaporation* and the neighboring boiling regime determined in.the experiments.

conductivity of the silicon wafer, the contact temperature between the drop and the substrate T_{cont} is theoretically estimated as a contact of two-infinite solid bodies by neglecting convection in the liquid as follows and taken as the vertical axis;

Fig. 4. *Tiptoeing* at very small impact velocity in a depressurized environment. $U_0 = 0.1$ m/s, $D_0 = 2$ mm, $p_{ch} = 2.5$ kPa (supplemental video 7). Substrate temperature is given in the first image. The scale bar shown in the first image is 2.0 mm. The contrast of the images has been enhanced.

$$T_{\text{cont}} = \frac{e_{\text{w}}T_0 + e_{\text{l}}T_1}{e_{\text{w}} + e_{\text{l}}}, \tag{1}$$

where e_{w} and e_{l} are thermal effusivity of the substrate and the liquid respectively. T_1 denotes initial drop temperature. The nozzle temperature has been controlled in the range of 15–35 °C; thus, T1 = 25 °C is taken in the following discussion. No special outcome is observed in the pressure range from 25 to 101 kPa for both impact velocities. The boundary temperature between *deposition* and *capillary rebound* tends to decrease along with a decrease in saturation temperature. This tendency has already been reported by Orejon et al. [38] for a static case and by van Limbeek et al. [39] for the dynamic case. Conversely, the ranges of substrate temperature for *vapor rebound* are significantly enlarged by increasing impact velocity from 0.1 to 0.46 m/s or by reducing the chamber pressure from 10 to 1 kPa. Interestingly, the threshold temperature between *vapor rebound* and *capillary rebound* becomes higher as p_{ch} decreases, even though the substrate superheating

temperature becomes larger due to the decrease in saturation temperature.

4. Kinematics of magic carpet breakup

Typical time evolution of the vertical position of the drop center of gravity in dimensionless form for the *magic carpet breakup* and *tiptoeing* regimes are shown in Fig. 6 in comparison with those of *capillary rebound* and *deposition*. The dimensionless vertical position $\xi = 2z_0/D_0$ is defined as the distance z_0 from the drop center of gravity to the substrate, normalized by the initial drop radius $D_0/2$. The moment when ξ becomes unity is taken as $t = 0$. The dimensionless time $\tau = tU_0/D_0$ is defined as the time t normalized by the typical time scale of drop impact. In the *magic carpet breakup* regime the drop exhibits a sudden backlash motion occurring at a velocity that may exceed the impact velocity, as shown in Figs. 3(d) and 6(a), or with a small deceleration followed by the second impact and a splash due to the drop inertia, as seen in Figs. 3(c) and 6(b). Interestingly, the backlash motion occurs only at relatively low temperatures in the *magic carpet breakup* regime, when considering only the first impact. On the other hand, the drop trajectory in the *tiptoeing* regime in Fig. 6(c) is similar to that of *capillary rebound*, even though small parts of the drop directly contact the substrate multiple times during the spreading phase.

Another feature of *magic carpet breakup* is the large deformation during the backlash motion or deceleration. Some examples of D_{max} measurements are shown in Fig. 7, where the test cases for which the measurement is conducted are clarified. The measurement is conducted for a limited region in the *magic carpet breakup* regime in which a detachment from the substrate is clearly observed after the first contact. The measurement is not conducted for the transition regime (the leftmost images in Fig. 7), since its physical mechanism is apparently different from the one presented in the present study. It is measured only for the images before the second impact, whereas a larger deformation may occur after the second impact. Fig. 8 shows the measurement result of D_{max} in dimensionless form. The dashed line in Fig. 8 indicates a typical value of $D_{\text{max}}/D_0 \approx 1.58$ for the same impact velocity in the deposition regime in a depressurized environment. This value is consistent with the existing model for a drop impacting onto a surface at room temperature under atmospheric conditions [55]. The dimensionless maximum diameter D_{max}/D_0 is shown to take a significantly larger value in the *magic carpet breakup* regime. Fig. 8 indicates that D_{max}/D_0 tends to decrease as the substrate temperature increases, whereas a peak is observed in the case of $p_{\text{ch}} = 5$ kPa. Interestingly, the dimensionless maximum diameter tends to become larger at $p_{\text{ch}} = 2.5$ kPa and 5 kPa compared to $p_{\text{ch}} = 1$ kPa.
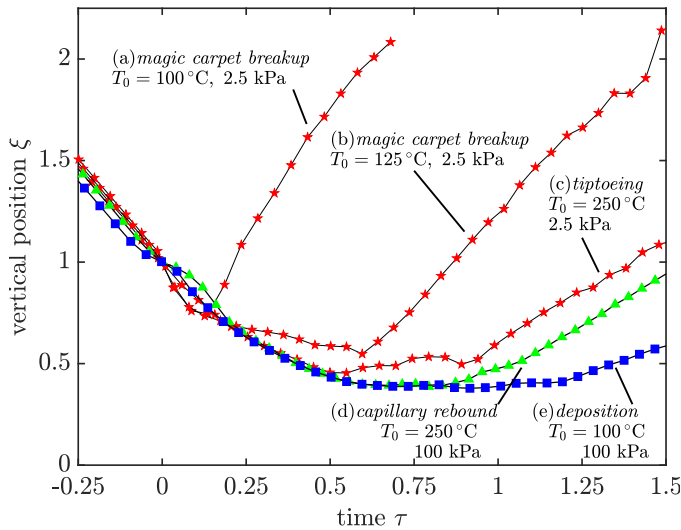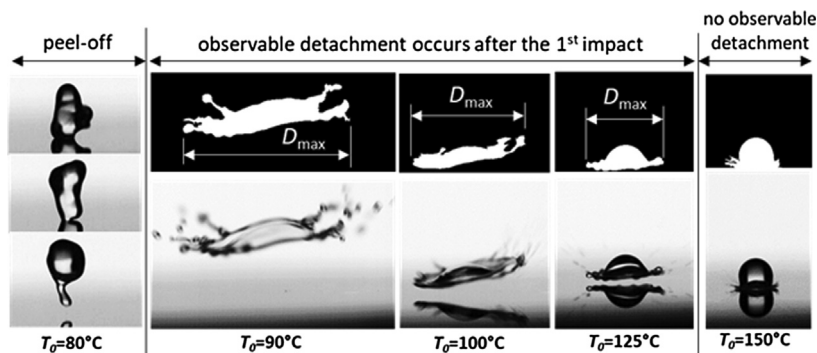

Fig. 6. Examples of the drop trajectories in the vertical direction for different drop outcomes. The impact conditions are similar for all cases: $U_0 \approx 0.46$ m/s, $D_0 \approx 2.0$ mm. The vertical position ($\xi = 2z_0/D_0$) is defined as drop center of gravity z_0 normalized by initial drop radius $D_0/2$, whereas time $\tau = tU_0/D_0$ corresponds to the typical time scale of drop impact. The moment $\tau = 0$ is defined as the moment when ξ is equal to one. The upward velocity after detachment from the substrate is (a) 0.52 m/s, (b) 0.41 m/s, (c) 0.25 m/s, (d) 0.17 m/s, respectively. Note that the trajectories shown here are not the average of multiple times of experiments but results of one time for each condition.

Fig. 7. Definition of the maximum spreading diameter (D_{max}) and the test cases for which the measurement is conducted. The measurement is conducted for a limited region in the *vapor rebound* regime, in which a detachment from the substrate is clearly observed after the first contact. The measurement is not conducted for the transition regime (the leftmost images). It is measured only for the images before the second impact, whereas a larger deformation may occur after the second. Test conditions of the images above; $p_{\text{ch}} = 2.5$ kPa, $U_0 = 0.46$ m/s. T_0 are given beneath each image. The contrast of the images has been enhanced.
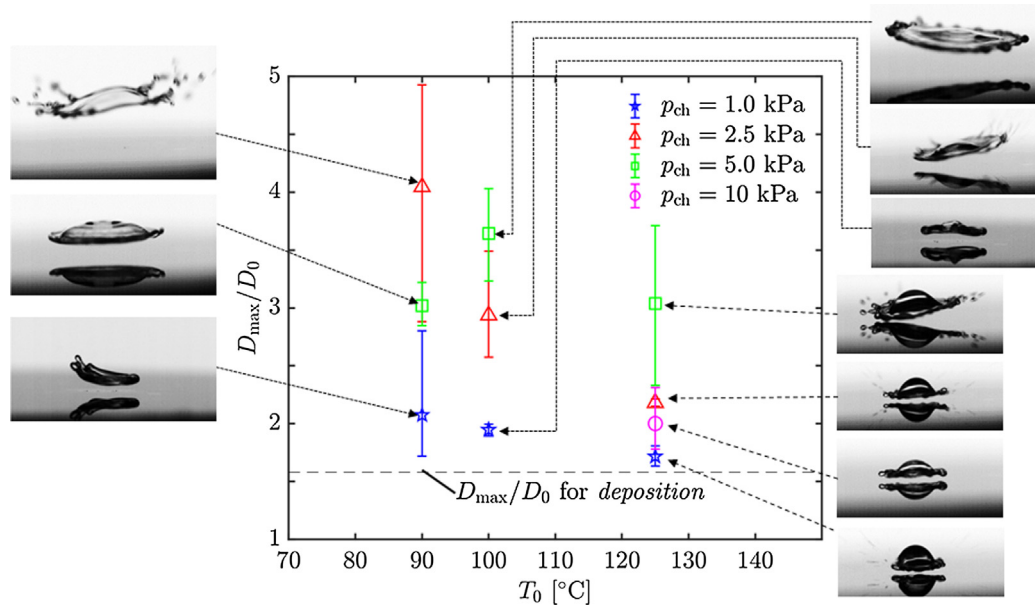
Fig. 8. Maximum spreading diameter (D_{max}) in the *magic carpet breakup* regime with observable detachment (see Fig. 7) normalized by initial drop diameter (D_0) at various substrate temperatures for different surrounding pressures. The dashed line indicates a typical value of D_{max}/D_0 at $U_0 \approx 0.46$ m/s in the *deposition* regime in our experiments. The error bars indicate the minimum and the maximum values over multiple experiments ($3 - 5$ times, depending on test case) for the same condition. One example of the drop image that is used for D_{max} measurement is shown for each condition. The contrast of the images has been enhanced.
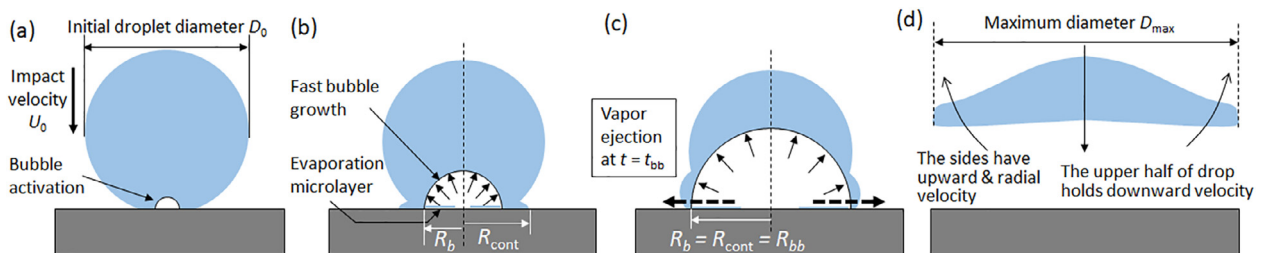

Fig. 9. Schematic illustration of *magic carpet breakup* caused by a single bubble bursting during the spreading phase after impact.

5. Hypothesis on the mechanism of magic carpet breakup

From the visual observations shown in Fig. 3(d) and the measurement results shown in Figs. 6 and 8, *magic carpet breakup* is considered to be caused by intensive vapor generation due to direct contact between the drop and the substrate. As the air cushion effect should be weaker under lower surrounding pressure, direct contact occurs even at relatively small impact velocities and relatively large substrate superheating. The bubble is expected to grow much larger in a depressurized environment than under atmospheric conditions [56]. In fact, visual observation has indicated in some cases that a bubble emerges at the contact surface, grows rapidly, and then finally bursts, resulting in significant drop deformation and upward motion.

Fig. 9 shows a schematic illustration of this process. As the bubble growth speed is supposed to be equivalent to the time scale of drop spreading, the time evolution of the contact radius R_{cont} between the drop and substrate is presumed to play an important role. The same bubble behavior was visually observed for *magic carpet breakup* that occurred on a rough surface under atmospheric conditions (c.f. Fig. 1). Although the bubble growth speed is limited at atmospheric pressure, the number of nucleation sites is much larger and the vapor bubbles generated from them presumably coalesce. This explanation is very similar to the Leidenfrost models

described in [23,24] that were established to estimate T_L from a given set of fluid and substrate properties, although the consequent drop deformation after detachment from the substrate has not been discussed.

As a hypothesis, bubble bursting is assumed to happen when the bubble radius R_b exceeds the contact radius R_{cont}, as shown in Fig. 9(c). Here the time and bubble radius at the moment of bursting are designated the bubble burst time t_{bb} and bubble burst radius R_{bb}, respectively. As the substrate temperature T_0 increases the bubble grows faster, leading to smaller t_{bb} and smaller R_{bb}. In such cases the drop deformation becomes smaller due to the limited bubble size and shape of the interface between the bubble and the drop. On the other hand, the bubble growth rate, which determines the radial velocity of liquid surrounding the bubble, increases as the T_0 increases, leading to larger drop deformation and upward motion. The detailed modeling of drop deformation and motion is out of scope in the present study, nonetheless these two opposite effects imply that both the deformation and upward motion peak under certain temperature conditions.

There are two major differences to the Leidenfrost model for atmospheric conditions proposed in [23,24]. First, in the present study the vapor bubble is assumed to grow from a single, entrained gas bubble at the center of the liquid-solid interface, whereas a number of vapor bubbles are assumed to grow simultaneously

from cavities on the substrate in the model of Bernardin and Muda-war [23,24]. There is a possibility that multiple bubbles start to grow simultaneously and coalesce into one large bubble, which may lead to smaller bubble burst times. Driscoll et al. [29] reported that a ring of microbubbles is entrapped around the impact center in addition to the central bubble when a drop impacts a surface at room temperature under depressurized environment. It is also known that a bubble ring, whose size is equivalent to the central bubble, form at the bottom surface of an impacting drop on a heated surface [57,58]. However, growth of the central bubble is presumed to be dominant, since it tends to have the maximum size, which leads to the smallest T_{req}, and the surrounding liquid heats up earlier due to the earlier contact. In fact Yu et al. [44] recently reported a direct observation of the bubble between the drop and the substrate by means of total internal reflection method under depressurized environment, in which only one bubble grows from the center. Second, the dynamic effect due to drop impact is taken into account in different ways. In our model, drop spreading motion is correlated with bubble growth based on a hypothesis in which the gas and vapor remain "trapped" in-between the drop and the substrate. In [24], the changes in fluid properties due to increased pressure at the interface caused by drop impact are taken into account. Roisman et al. [59] theoretically estimated the time evolution of inertial pressure after drop impact. By adopting their model, the initial pressure can be calculated in the order of a few hundred Pascals at the present experimental conditions ($U_0 \approx 0.46$ m/s). This pressure rise is equivalent to the minimum surrounding pressure in our experiment, however it decreases rapidly with time. Although it may affect the pressure condition in the bubble a short time after impact, we neglected it in this analysis for the sake of simplicity.

The hypothesis presented in this section defines the strategy of the modeling. We estimate the waiting time for bubble activation, compute the bubble growth rate, and compare the bubble diameter with the contact diameter. If the bubble exceeds the contact diameter it will burst.

6. Theoretical analysis

6.1. Threshold temperature for bubble activation

Conditions for bubble activation are theoretically explained in many textbooks such as [60]. A bubble on a heated surface grows when $p_v + p_{NCG} > p_l + 2\sigma/r_c$, where p_v denotes the internal vapor pressure, p_{NCG} denotes the pressure of non-condensable gas in the bubble, p_l denotes the surrounding liquid pressure (approximately equal to the chamber pressure p_{ch}), σ denotes the surface tension of water, and r_c denotes the cavity radius of the nucleation site. The gas composition in the cavity is considered to be similar to that of the surrounding gas in the chamber, which is difficult to estimate since air-tightness of the chamber is not perfect. For the sake of simplicity, we assume $p_{NCG} = 0$ by considering that the air in the chamber is sufficiently replaced with water vapor during the degassing phase. Pressure and temperature of fluid on the saturation curve has a non-linear relationship described with the Clausius-Clapeyron equation, which can be simplified as $dp/p = (L/\mathcal{R}_{H_2O})(dT/T^2)$ where $\mathcal{R}_{H_2O}$ denotes the universal gas constant of water vapor, L denotes the specific latent heat of evaporation, p denotes pressure, and T denotes temperature. Here we define the threshold vapor temperature T_{req} above which a bubble starts to grow and the corresponding vapor pressure p_{req}. By integrating the simplified Clausius-Clapeyron equation along the saturation curve from p_{ch} to p_{req} and the corresponding temperatures from T_{sat} (the saturation temperature at p_{ch}) to T_{req}, the threshold

superheating temperature $\Delta T_{req} = T_{req} - T_{sat}$ can be calculated as follows [60]:

$$\Delta T_{req} = \frac{\mathcal{R}_{H_2O} T_{sat} T_{req}}{L} \ln \frac{p_{req}}{p_{ch}} = \frac{\mathcal{R}_{H_2O} T_{sat} T_{req}}{L} \ln \left(1 + \frac{2\sigma}{p_{ch} r_c}\right), \qquad (2)$$

By solving Eq. (2) with $\Delta T_{req} = T_{req} - T_{sat}$, the required substrate temperature finally leads to:

$$T_{req} = \frac{T_{sat}(p_{ch})}{1 - \frac{\mathcal{R}_{H_2O} T_{sat}(p_{ch})}{L} \ln \left(1 + \frac{2\sigma}{p_{ch} r_c}\right)}. \qquad (3)$$

The vapor in the cavity (or entrapped bubble as discussed later) is considered to take the temperature between the initial drop temperature and the substrate temperature at the beginning, and then converge to the latter. Therefore, if the observation time is sufficiently long, T_{req} can be interpreted as the required substrate temperature for bubble activation. Since an activated bubble tends to grow very large in a depressurized environment, we can recognize whether the bubble activation has occurred by visual observation. Thick arrows in Fig. 5 express the threshold between *film evaporation*, in which no bubble generation is observed, and the neighboring boiling regime (e.g. *nucleate boiling*). When bubble generation is observed at the lowest temperature, the arrow is drawn just below the lowest temperature. Note that the threshold indicated with arrows is not coincident with the regime boundary in Fig. 5, as drop outcomes in this paper are categorized based on drop motion rather than boiling state.

Since the influence of p_{ch} on T_{sat} is moderate, Eq. (2) indicates that ΔT_{req} becomes larger as p_{ch} becomes smaller, which qualitatively agrees with the trend observed in the experiments. However, the required substrate temperature T_{req} takes a very large value when r_c is assumed to be equivalent to the surface roughness of silicon wafer (on the order of a few nanometers), which obviously disagrees with the experimental result. The visual observation of bubble generation in the experiments indicates the existence of micron-sized cavities. The dashed curve expresses T_{req} estimated in Eq. (3) by adopting $r_c = 7.0$ μm, so that the curve roughly fits the arrows. One possible explanation of the estimated cavity size of $r_c \approx 7.0$ μm is that a small bubble is entrained during the impact [61–64], which will act as a nucleation site [65]. The entrained gas layer initially has a very thin disk shape and then retracts into a spherical bubble at the center, with a time scale of a few tens of microseconds. Here we assume that the spherical bubble, rather than the thin gas layer, becomes a nucleation site and is activated due to heat conduction from the substrate, since the time scale of the retraction is smaller than the time scale of *magic carpet breakup* and still equivalent to it even in the *tiptoeing* regime. The typical size of the central bubble after the retraction is about a few tens of micrometers for a millimeter drop under atmospheric conditions. Li et al. [36] reported that the radius and thickness of an air bubble entrained during drop impact in a depressurized environment decreases as pressure decreases. The result is less than 160 nm in thickness and 51 μm in diameter at 2.8 kPa, which will transform into a central bubble with the diameter of approximately 6.7 μm after retraction. Therefore, the estimated radius of the nucleate bubble in our experiments is consistent with their measurement result. In the latter discussion, the cavity radius r_c is fixed at 7.0 μm for the sake of simplicity.

6.2. Waiting time for bubble activation

As the drop size is three orders larger than the estimated cavity size, the waiting time t_w, which is the time duration from the moment when subcooled liquid contacts the superheated surface to the moment when the nucleate bubble starts to grow, can be estimated in the same manner as pool boiling. The waiting time

t_w is estimated by solving a semi-infinite heat conduction problem as [66,67]:

$$t_w = \frac{1}{4\alpha_l}\left[\frac{r_c}{\text{erfc}^{-1}\left(\frac{T_{req}-T_l}{T_{cont}-T_l}\right)}\right]^2.$$

(4)

Here α_l denotes to the thermal diffusivity of liquid water. Eq. (4) corresponds to the time duration until the top edge of a nucleate bubble with radius r_c reaches T_{req}. By assuming $r_c = 7.0\,\mu m$, as discussed in Section 6.1, t_w can be calculated for each experimental condition. When the substrate temperature T_0 increases, the waiting time t_w rapidly decreases and finally converges to a small value, which is smaller than the time resolution of the observation $t \sim 0.2$ ms.

6.3. Bubble growth model

6.3.1. Existing model for pool boiling

The bubble growth on a heated wall in a liquid pool, generally referred to as bubble growth in a non-uniform temperature field, has been extensively studied in the past. There are two known modes of bubble growth: inertia-controlled growth, in which the growth rate is governed by the momentum interaction between the bubble and the surrounding liquid, whereby heat transfer to the interface is sufficiently fast; and heat-transfer-controlled growth, in which it is limited by the slower transport of heat [67].

An important dimensionless number that determines the bubble growth mode is the Jakob number (designated as Ja) which expresses how much vapor will be generated by liquid-vapor phase change given a certain superheating of the liquid. By assuming the inverse linear relationship between vapor density ρ_v and surrounding pressure p_{ch} the Jakob number Ja can be calculated as follows [67]:

$$Ja = \frac{c_{pl}\,\rho_l(T_0-T_{sat})}{\rho_v L} \approx \frac{c_{pl}\,\rho_l\,p_0\,(T_0-T_{sat})}{\rho_{v0}\,p_{ch}\,L},$$

(5)

where p_0 denotes the atmospheric pressure, c_{pl} denotes the specific heat of liquid, and ρ_{v0} denotes the saturated vapor density at atmospheric pressure. ρ_v and ρ_l denote the vapor and liquid density at chamber pressure p_{ch} respectively. Note that Ja becomes extremely high (in the range of $Ja \approx 1500-68000$) in the *vapor rebound* regime due to the depressurized environment and relatively large superheating as compared with a pool boiling experiment.

Mikic et al. [68] presented a simple theoretical model for bubble growth in an extensive uniformly superheated liquid pool (i.e. isothermal condition) that covers both the inertial-controlled regime and heat-transfer controlled regime and extended it to the bubble growth onto a heated surface that involves non-uniform temperature field [66,68]. Their analytic result for the isothermal case is in very good agreement with experimental results for a depressurized environment (Ja = 2690 at surrounding pressure of 1.2 kPa) reported by Lien [69]. The range of Ja in the present work is far larger than the range in which the validity of the model has been confirmed; nonetheless, the model basically has no restrictions regarding Ja. Thus their model is employed to determine the bubble growth mode. In their model a dimensionless time t^+ is defined as:

$$t^+ = \frac{t}{(B/A)^2},$$

(6)

where

$$A = \left[\frac{\pi}{7}\frac{L\rho_v(T_0-T_{sat})}{\rho_l T_{sat}}\right]^{1/2},$$

(7)

$$B = \left(\frac{12}{\pi}\alpha_l\right)^{1/2} Ja.$$

(8)

As Mikic et al. [68] presented, inertia-control bubble growth is dominant when $t^+ < 1$, whereas heat-transfer-control bubble growth is dominant when $t^+ > 1$. When the discussion focuses on the *vapor rebound* regime, the dimensionless time t^+ takes a very small value lying between 10^{-4} to 10^{-1} depending on T_0 and p_{ch} when the typical time scale of drop impact $t = R_0/U_0 \approx 2.0$ ms is employed in Eq. (6). Thus, the effect of heat-transfer controlled growth can be neglected below 10 kPa, not only in the early stage, but also during the entire process of bubble growth until the bubble bursts.

van Stralen et al. [56] performed pool boiling experiment on a heated wall in a depressurized environment (2.0–26.7 kPa) and reported that the previously proposed models that take liquid inertia into account are in good agreement for the early stage of bubble growth. Among them, the model proposed by Mikic et al. [68] is derived from the kinetic energy balance and describes the bubble growth rate A simply with Eq. (7). van Stralen et al. [70] empirically included a decay of surface temperature due to evaporation by substituting the superheating temperature $(T_0 - T_{sat})$ in Eq. (7) with $(T_0 - T_{sat})e^{(-t/t_1)}$. Here t_1 denotes the bubble departure time, based on experimentally observed temperature fluctuation in the heating rod.

These models are not directly applicable to the current problem due to the following reasons. Firstly the mass of the surrounding liquid is much smaller in case of bubble growth in a drop than that in a liquid pool. Secondary, these models are derived from linearized form of Clausius-Clapeyron equation, in which the fluid properties at the saturation point are used. Some researchers [71,72] claimed that the error due to the linearization becomes significantly large when the superheating temperature is large. Finally, thermal effect are not directly taken into account in those models. The vapor temperature is assumed to be identical to the surface temperature, which is assumed to be the same as substrate temperature in [68] and is empirically modeled by [70] as mentioned previously. Considering the larger gradient of saturation curve (P_{sat}-T_{sat} curve) at higher temperature and relatively smaller thermal conductivity (or effusivity) of silicon than that of copper used in [56], the modeling of vapor temperature and surface temperature is important to estimate the bubble growth rate in the current problem.

Thus, a new bubble growth model for a drop impacting onto a heated surface under depressurized environment is developed in the following sections. This problem is extremely complicated and not yet solved. There are several different approaches, but in this study we consider the inertia-controlled growth as a probably major mechanism, and thus develop a model by extending the
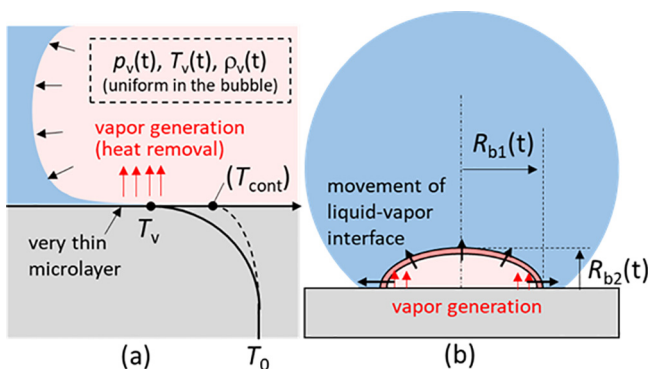

Fig. 10. The schematic illustration of heat transfer and temperature profile in the substrate during growth period of inertia-controlled bubble growth. The dashed line in (a) indicates preexisting temperature field formed in the waiting period.

existing models mentioned above. The probable influence of a thin liquid layer beneath the bubble [73], transient readjustment of temperature field in the wall [74], the wetting effect [75,76], and the air cushion effect [27,28] are currently neglected.

6.3.2. Heat and mass balance

A schematic illustration of the thermal model is shown in Fig. 10. The model is one-dimensional as shown in Fig. 10(a), whereas the volume of bubble is calculated as a semi-ellipsoid as shown in (b) taking into account the difference in bubble growth rate between in horizontal and vertical directions. The vapor in the bubble is under two-phase equilibrium state, thus the vapor pressure p_v and the vapor temperature T_v are correlated by the Clausius-Clapeyron equation. An approximate expression for the saturation curve is used to avoid an error due to linearization. The driving force of bubble growth is the pressure difference $p_v(T_v) - p_{ch}$, thus the vapor temperature T_v is a key factor that determines the bubble growth rate.

When the evaporation starts, the temperature at the liquid-vapor interface where the evaporation occurs (named evaporation front) drops to a certain temperature, which is generally considered to be equal to the saturation temperature $T_{sat}(p_{ch})$ for nucleate boiling under atmospheric conditions [66,67]. In contrast, in the inertia-controlled growth regime, p_v is determined by momentum interaction between the vapor and surrounding liquid, thus the interface temperature takes the saturation temperature $T_v(p_v)$ that is significantly higher than $T_{sat}(p_{ch})$. Evaporation is supposed to occur mainly around the receding contact line where the thickness is a minimum. For the sake of simplicity, it is assumed here that evaporation occurs only on the top surface of a very thin evaporation microlayer or at the edges of the triple contact line, in which the temperature difference between evaporation front and the solid surface is negligible. The heat transfer along the dome-shaped liquid-vapor interface is also neglected, thus the heat removal due to evaporation is compensated solely by the heat conduction through the thermal boundary layer in the substrate. The heat flux is estimated as follows;

$$q_1 \approx \frac{e_w(T_0 - T_v)}{t^{1/2}}, \tag{9}$$

Note that the effect of the preexisting thermal boundary layer formed in the waiting period, which is also illustrated in Fig. 10, is neglected in Eq. (9) for the sake of simplicity. On the other hand, the averaged heat flux at the bottom face of the bubble due to evaporation can be estimated from the mass evaporation rate by assuming hemi-ellipsoidal bubble shape:

$$q_2 = \frac{(dV/dt)\rho_v L}{\pi R_{b1}^2} = \frac{2\rho_v L}{3R_{b1}}(2R_{b2}A_1 + R_{b1}A_2), \tag{10}$$

where V, R_{b1}, and R_{b2} denote the volume, horizontal radius, and vertical radius of the bubble, respectively. $A_1 = dR_{b1}/dt$ and $A_2 = dR_{b2}/dt$ denote the bubble growth rate in the horizontal and vertical directions respectively. On the other hand, by using the relationship $q_1 = q_2$ and $\rho_v \approx \rho_{v0}(p_v/p_0)$ the following relationship is obtained.

$$\frac{e_w(T_0 - T_v)}{t^{1/2}} \approx \left(\frac{p_v}{p_0}\right)\frac{2\rho_{v0}L}{3R_{b1}}(2R_{b2}A_1 + R_{b1}A_2), \tag{11}$$

6.3.3. Kinetic interaction between the bubble and surrounding liquid

The kinetic interaction between the bubble and the surrounding liquid in the inertia-controlled growth can be described in the same manner as pool boiling [68], where a literature value for the total kinetic energy for the liquid surrounding a growing bubble $E_{kin,l}$ on a flat surface in a liquid pool is used. The momentum equation is complicated due to the absence of spherical symmetry. The value is approximately 1.49 times larger than $E_{kin,l}$ for the spherical symmetry case that is calculated theoretically. We assume here that the ratio of $E_{kin,l}$ is almost the same between the case in which a spherical bubble grows in a spherical drop, shown in Fig. 11(a), and the case in which a hemispherical bubble grows in a hemispherical drop, shown in Fig. 11(b). The non-uniformity of liquid distribution is not directly modeled, but taken into account by substituting the radius of hemisphere with two different values (R_{cont} and $2R_0$).

The total kinetic energy of the liquid phase $E_{kin,l}$ in Fig. 11(b) at an arbitrary time can be roughly estimated as follows by extending the model in [68] as described above.

$$E_{kin,l} = 1.49 \times \frac{\rho_l}{2}\int_R^{R_{lim}} u_r^2 dV = 9.35\rho_l\left(\frac{dR_b}{dt}\right)^2 R_b^3(1 - \epsilon) \tag{12}$$

where R_{lim} denotes the drop radius in the model shown in Fig. 11(b) and $\epsilon \equiv R_b/R_{lim}$ denotes bubble size ratio. u_r denotes the radial velocity of liquid. On the other hand, the net work done by a growing hemispherical bubble to the surrounding liquid (Fig. 11(b)) can be estimated as follows by neglecting the pressure drop across the liquid-vapor interface [67,68];

$$W = 2\pi\int_0^{R_b}(p_v - p_{ch})R^2 dR \approx \frac{2}{3}\pi R_b(p_v - p_{ch}) \tag{13}$$

The last expression is obtained by successive integration by parts and taking only the first part, assuming that the derivative of vapor pressure ($\frac{dp_v}{dR}$) is small during the bubble growth [68]. By equating Eq. (12) with Eq. (13), one obtains:

$$A = \frac{dR_b}{dt} = \left[\frac{\pi}{14(1 - \varepsilon)}\left(\frac{p_v - p_{ch}}{\rho_l}\right)\right]^{1/2} \tag{14}$$
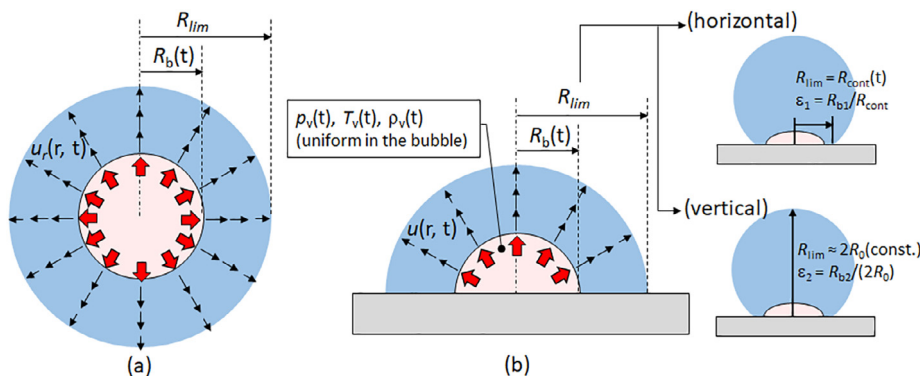

Fig. 11. Schematic illustrations of kinetic interaction during a bubble growth in a drop. (a) Spherical bubble growth from the center of spherical drop, (b) hemispherical bubble growth in a hemispherical drop on a flat surface.

The horizontal bubble growth rate A_1 can be estimated by taking $\epsilon_1 = R_{b1}/R_{cont}$, whereas the vertical growth rate A_2 can be estimated by taking $\epsilon_2 \approx R_{b2}/(2R_0)$. A_1 is expected to be larger than A_2 since R_{cont} is usually smaller than $2R_0$, leading to larger R_{b1} than R_{b2}.

6.4. Drop spreading

The time evolution of contact radius $R_{cont}(t)$ (generally referred as spreading radius in the literature) has been extensively investigated mainly for room temperature surfaces. Rioboo et al. [77] presented an empirical model ($R_{cont}/R_0 = (3.92tU_0/R_0)^{1/2}$) for the early (kinematic) phase of impact, which is independent of the wettability between the liquid and the surface. Riboux and Gordillo [78] presented a theoretical estimation ($R_{cont}/R_0 = (3tU_0/R_0)^{1/2}$) and confirmed a very good agreement with experimental results for high Weber number. On the other hand for low Weber number de Goede et al. [79] presented a model for the maximum spreading radius in which the capillary effect is taken into account, however the time evolution of R_{cont} is not given in their model. Therefore, in the present study, the empirical model proposed by Rioboo et al. [77] is employed as follows:

$$R_{cont}(t) = \sqrt{3.92R_0U_0t} \qquad (15)$$

R_{cont} is assumed here to be independent of bubble growth, and thus calculated separately.

6.5. Step by step calculation of bubble growth and bursting

Eqs. (11) and (14) can be numerically solved with fixed values of R_{b1}, R_{b2}, and R_{cont} at each time step and one can obtain the estimations of A_1, A_2, and p_v at that moment. By conducting step by step calculation from the initial conditions of $t = t_w$ and $R_{b1} = R_{b2} = 0$ and updating R_{b1} and R_{b2} by using calculated A_1 and A_2, one obtains the time evolution of R_{b1} and R_{b2}. Fig. 12 shows some examples of the numerical result for bubble growth curve under the same substrate temperature $T_0 = 125\,°C$ under various pressure condition, accompanied by the evolution of R_{cont} calculated in Eq. (15). The x-coordinate of the starting point of the bubble growth curve corresponds to the waiting time t_w, and the x- and y-coordinate of the crossing point of R_b and R_{cont} are named the bubble burst time t_{bb}.
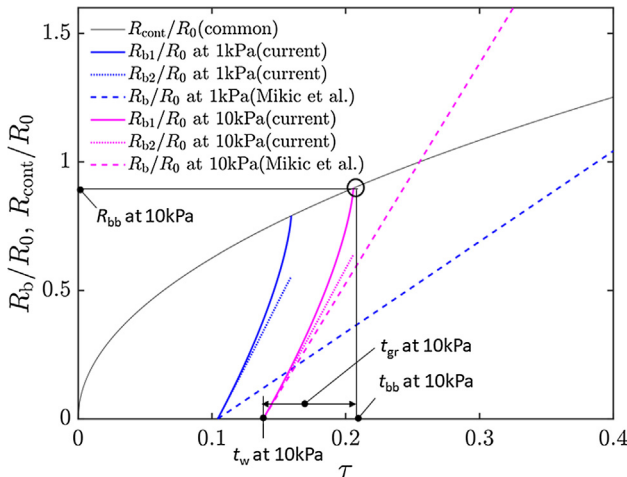

Fig. 12. Time evolution of contact radius (R_{cont}) and bubble radius (R_b) under two different pressure conditions: $T_1 = 25\,°C, R_0 = 0.001\,m, U_0 = 0.46\,m/s, r_c = 7.0\,\mu m$, $T_0 = 125\,°C$ ($T_{cont} = 112.3\,°C$). R_{cont} is calculated in Eq. (12) for all cases. The solid and dotted curves are numerical result by Eq. (11), whereas the dashed curves are the analytical result by Eq. (7) based on the model by Mikic et al. [68]. The waiting time (t_w) is calculated with Eq. (4) for all cases. The crossing points of the bubble radius and contact radius curve correspond to the bubble burst time (t_{bb}).

and bubble burst radius R_{bb}, respectively. t_{gr} denotes the bubble growing time, which is defined as $t_{gr} = t_{bb} - t_w$ as shown in Fig. 12. This graph indicates that the model gives the larger bubble growth rate compared to the model by Mikic et al. [68] shown in Eq. (5), especially when the chamber pressure p_{ch} is extremely low. This is because Eq. (7) tends to underestimate the vapor pressure due to linearization of Clausius-Clapeyron equation and the usage of fluid parameters at p_{ch}, whose error becomes more significant as the chamber pressure decreases. The bubble growth in horizontal direction accelerates before the bubble bursting due to the increase in ϵ_1, whereas the growth in the vertical direction is almost constant due to sufficiently small ϵ_2 in the case of Fig. 12. The influence of the environmental pressure p_{ch} on the bubble growth curve is not significant in the current model, since the vapor pressure is basically determined by the surface temperature. This trend comes from the formulation of Eqs. (11) and (14) in which the system pressure p_{ch} only emerges as the pressure difference ($p_v - p_{ch}$). p_v tends to be much larger than p_{ch} in most cases for the *vapor rebound* regime leading to $p_v - p_{ch} \approx p_v$ except for conditions around the lowest temperature at 10 kPa. The vapor density is influential in the energy balance (Eq. (10) or Eq. (11)), however it is relevant to p_v instead of p_{ch}.

6.6. Drop velocity after bubble bursting

The upward force applied to the drop by the growing bubble to the drop can be roughly estimated as follows:

$$F_v = (p_v - p_{ch})\pi R_{b1}^2, \qquad (16)$$

where πR_{b1}^2 expresses the projected area of the bubble. The drop velocity after the bubble bursting U_1 can be estimated as follows;

$$U_1 = U_0 - \frac{1}{m_{drop}} \int_{t_w}^{t_{bb}} F_v dt, \qquad (17)$$

where $m_{drop} = \frac{4\pi}{3} R_0^3 \rho_l$ denotes the total mass of the drop and U_1 denotes the drop velocity after the bubble bursting. The numerical analysis described in the last section gives us an estimation of p_v, R_{b1} at each moment and t_{bb}, thus one obtains an estimation of U_1 by performing step by step integration from t_w to t_{bb}.

7. Comparison with experiment

The numerical result for the bubble burst time as a function of the contact temperature under various pressure conditions are shown in Fig. 13 in dimensionless form, accompanied by the experimental results in the *vapor rebound* regime. Note that the transition regime shown in Figs. 3(e) and 7 is excluded, since this mode is apparently driven by a different mechanism from Fig. 9. The illustrations on the right show the drop shape evolution observed in the *deposition* regime ($p_{ch} = 101\,kPa, T_0 = 100\,°C$) at each dimensionless time. The bubble burst time t_{bb} of the experiment is determined by visual observation, whose time resolution is 0.2 ms, corresponding to the frame rate of 5000 fps. If a splash (shadow of tiny liquid droplets) is observed in the first frame, t_{bb} is determined as $t = 0.1$ ms, halfway between 0 ms and 0.2 ms. The moment of impact $t = 0.0$ ms is adjusted by measuring the distance between the bottom edge of the drop and the substrate in the previous image, dividing it with the impact velocity, and subtracting it from measured t_{bb}. The error bars indicate the root mean square error of the maximum error from the averaged value and the half of the time between two successive images. The bubble burst time decreases by increasing the substrate temperature, and soon becomes less than the time resolution. The analytical results exhibit good quantitative agreement with the experimental results, even though no fitting parameter is employed in the anal-
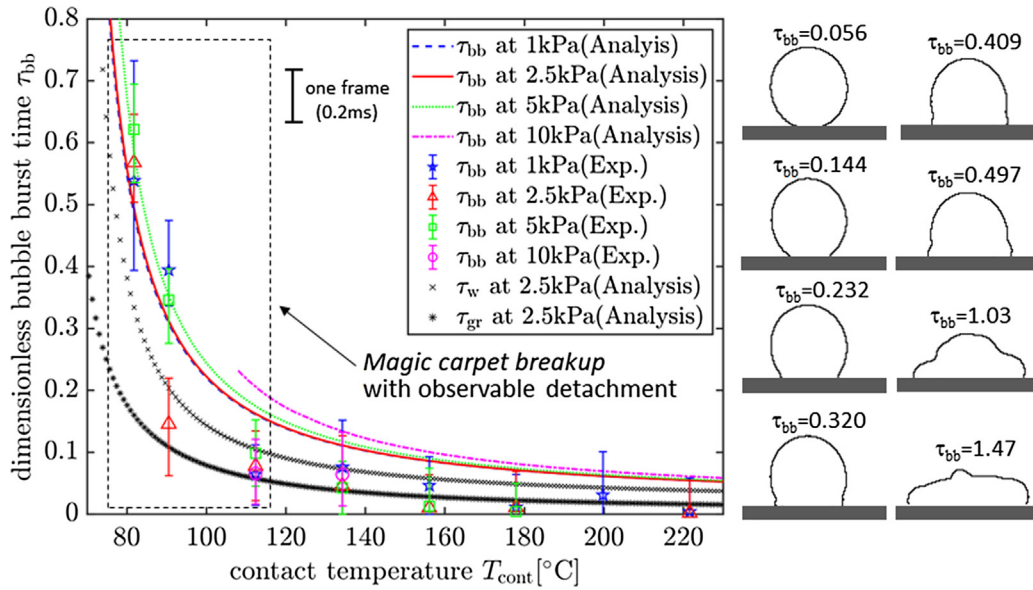
Fig. 13. Numerical results of dimensionless bubble burst time ($\tau_{bb} = t_{bb}U_0/D_0$) for *vapor rebound* regime except for the transition regime. $T_1 = 25\,°C, R_0 = 0.001\,m, U_0 = 0.46\,m/s, r_c = 7.0\,\mu m$. The contact temperature T_{cont} (the horizontal axis) is calculated by (1). The contributions of $\tau_w = t_wU_0/D_0$ and $\tau_{gr} = t_{gr}U_0/D_0$ to τ_{bb} in the analysis are shown only for $p_{ch} = 2.5\,kPa$ with two black markers. The experimental results are also indicated by the markers. The error bars indicate the root mean square error of the maximum error from the averaged value and the half of the time between two successive images.

ysis except for the cavity radius r_c, which is not fitted in Fig. 13 but in Fig. 5, as explained in Section 6.1. Only a small influence of the p_{ch} is seen, because the vapor pressure in the bubble takes a much larger value: e.g. $p_v = 30\,kPa$ at $T_v = 70\,°C$. The analysis expects a larger contribution of the waiting time τ_{bb} than that of the growth time τ_{gr} for all temperature ranges as indicated by the black markers, whereas there is no experimental information on the attributable proportion. It is noteworthy that the analysis tends to overestimate τ_{bb} for higher T_{cont}. The slight difference in τ_{bb} at small τ_{bb} leads to significant difference in the bubble burst radius R_{bb} as indicated by the illustration in Fig. 13.

The numerical results on the velocity change U_1/U_0 for the cavity radius $r_c = 7.0\,\mu m$ are shown in Fig. 14. U_1 is experimentally measured and shown in the graph by the markers only in the *magic carpet breakup* regime with observable detachment (c.f. Fig. 7), since the drop velocity after the first splash but before the second contact couldn't be measured for the others. The trend estimated by the analysis qualitatively agrees with experiments, in which the drop has negative velocity when the substrate temperature is relatively low and the ratio U_1/U_0 may exceeds the initial drop velocity U_0. Although p_v decreases as T_{cont} decreases, the opposing effects, i.e. increase in R_b and t_{bb}, seem to be dominant, leading to the sharp increase in U_1. Nonetheless the analysis tends to overestimate the velocity change for all temperature range. Especially the threshold temperature for the backlash estimated by the analysis is much higher than that of experiment.

These discrepancies, i.e. the overestimation of t_{bb} in the higher temperature regime and that of U_1 in all temperature ranges, imply overestimation of bubble growth rate and τ_w. The growing bubble in the drop is basically hidden in the shadow of the drop, therefore the direct measurement of R_b is principally not possible in the *vapor rebound* regime in this study. Nonetheless, the measurement is conducted for an experimental condition for the *deposition* case in which the bubble is relatively clearly observable, as shown in Fig. 15, in order to check the validity of the model. R_{b1} is simply measured as the half length of the bubble in the horizontal direction, as shown in the images by neglecting the refraction at the drop surface. The measurement results are shown in Fig. 16. This
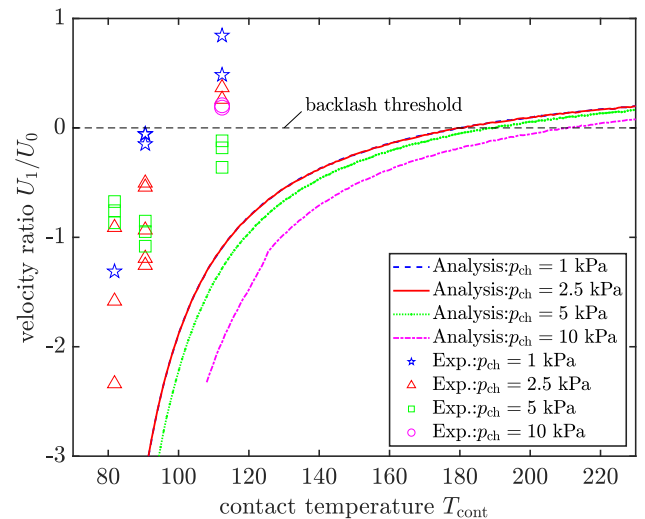

Fig. 14. Analytical results of the velocity ratio U_1/U_0 calculated by Eq. (14). $r_c = 7.0\,\mu m, R_0 = 1.0\,mm, U_0 = 0.46\,m/s$. The contact temperature T_{cont} (the horizontal axis) is calculated by Eq. (1). Experimental results in the *magic carpet breakup* regime with observable detachment are also indicated by the markers. If the U_1/U_0 takes the positive value the drop will impacts the surface again.

result also implies that the current model tends to overestimate both A and t_w.

There are some possible reasons that may explain this. First, the radius of the nucleate bubble is determined by visual observation of the required contact temperature for bubble activation, however the variation in the experimental result (thick black arrows in Fig. 5) are not small and the observation time is quite limited (a few milliseconds). Underestimation of r_c leads to overestimation of t_w due to overestimation of T_{req}, whereas it may be influential in the opposite direction, since r_c is in the numerator in Eq. (4). It is derived based on one-dimensional transient heat conduction model, however it may be necessary to develop a new model considering the time evolution of nucleate bubble shape and liquid
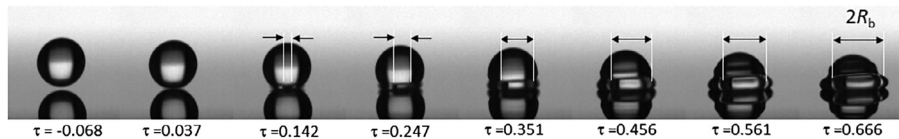
Fig. 15. Bubble growth in the drop in *deposition* regime. $R_0 = 0.88$ mm, $U_0 \approx 0.46$ m/s, $T_1 \approx 25$ °C, $T_0 = 100$ °C ($T_{cont} \approx 90$ °C).
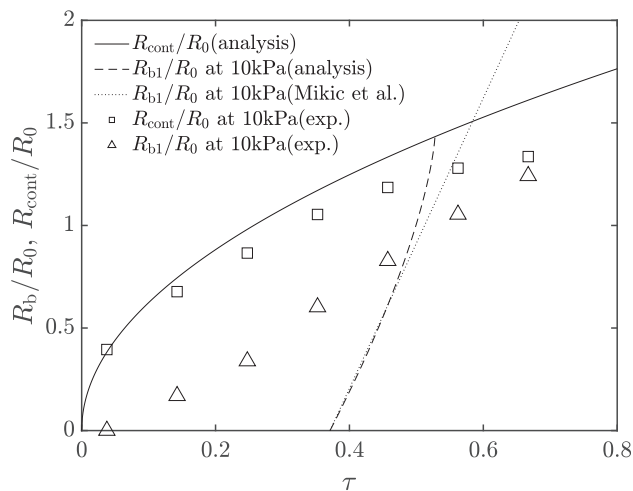

Fig. 16. Experimental result of contact radius (R_{cont}) and bubble radius (R_b) in *deposition* regime in dimensionless form. $R_0 = 0.88$ mm, $U_0 \approx 0.46$ m/s, $T_1 \approx 25$ °C, $T_0 = 100$ °C($T_{cont} \approx 90$ °C). The numerical results and the result of Eq. (5) by Mikic et al. [68] at $r_c = 7.0$ μm. are also shown.

flow. Second, the current thermal model neglects the temperature difference between the vapor and the solid surface, however it may becomes significant due to the thermal resistance in the evaporation microlayer. The thickness is expected to be of the order of a few to ten micro-meters based on the model of [67,70] for pool boiling, which leads to significant temperature difference if it is uniformly distributed. Likewise, the temperature difference may occur also by a slight difference in the microscopic thickness distribution at triple contact line [73]. Superheated relaxation microlayer [67,70] or condensation [80,81] along the dome of the bubble may also play an important role.

8. Conclusion and remarks

In the present study an experimental investigation of single drop impact onto a heated surface in a depressurized environment is described. Regime maps of drop outcomes over a wide range of surrounding pressure from 1 to 101 kPa for two different impact velocities were presented, and a new outcome named *vapor rebound*, which is subdivided into *magic carpet breakup* and *tiptoeing*, has been identified. *Vapor rebound* occurs in a temperature range between *deposition* and *capillary rebound* and only at relatively low surrounding pressures. The range of substrate temperature and surrounding pressure for *vapor rebound* becomes wider as the surrounding pressure decreases or as the impact velocity increases. In the *vapor rebound* regime, a drop tends to deform more extensively as the substrate temperature decreases. The threshold temperature for the onset of boiling is much lower than that estimated with the roughness level of the substrate, which implies that an air bubble entrapped during impact acts as a nucleation center.

A hypothesis on the mechanism of *magic carpet breakup* has been proposed, based on a bubble growth model correlated with the spreading motion of a drop. A theoretical model for a bubble growth in a drop attached onto the heated substrate is newly developed.

The numerical results of bubble burst time (τ_{bb}) and upward drop velocity (U_1/U_0) qualitatively agree with the experimental results. The counter-intuitive trends, i.e. the velocity change and drop deformation becoming larger as the substrate temperature becomes smaller and the upward drop velocity sometimes exceeding the impact velocity, can be explained by the model proposed in this study. Nevertheless, the model tends to overestimate both τ_{bb} and U_1/U_0, which implies the overestimation of bubble growth rate and/or of the waiting time. More direct experimental observation of the growing bubble, e.g. total internal reflection (TIR) imaging [44,82], is necessary for the further discussion.

As a future perspective, the following points are to be discussed. First, the air cushion effect is supposed to influence R_{cont} and t_w in the very early phase of drop impact. It has been studied for room temperature surfaces [27,28], nonetheless it is not sufficiently understood for heated surfaces. Second, the onset of nucleate bubbles and their activation is influenced by the surface contamination and noncondensable gas in the ambient gas, both of which are not sufficiently controlled in the current study due to experimental difficulties. Third, the time evolution of the contact radius (R_{cont}) is supposed to be influenced by the growing bubble, though it is assumed to be the same as that for room temperature drop impact in this study. The movement of the receding contact line (outer edge of bubble) as well as the thickness distribution of the evaporation microlayer may be key factors that determine the vapor pressure. The physical mechanism of those have been studied for decades for pool boiling, however there is no report on these mechanism for drop impact. The application of special measurement techniques, e.g., frustrated total internal reflection imaging (FTIR) [82] and thin-film thermocouple [80,83], to this problem may provide insight for better understanding. Finally, readjustment of the temperature field in the heated substrate due to the sudden emergence of bubbles (i.e. poor heat conductor) [74] may be another key factor to estimate the temperature at the vaporization front. The problem is extremely complicated, thus more experimental information and further theoretical consideration based on different modeling approaches are necessary.

Declaration of Competing Interest

There are no conflict of interest in this work.

Acknowledgement

Appendix A. Supplementary material

Supplementary data associated with this article can be found, in the online version, at https://doi.org/10.1016/j.ijheatmasstransfer.2019.118729.

References

[1] J. Kim, Spray cooling heat transfer: the state of the art, Int. J. Heat Fluid Flow 28 (2007) 753–767.

[2] J. Naber, R. Reitz, Modeling engine spray/wall impingement, SAE Trans. 97 (1988) 118–140.

[3] H. Zhang, W. Tao, Y. He, W. Zhang, Numerical study of liquid film cooling in a rocket combustion chamber, Int. J. Heat Mass Transf. 49 (2006) 349–358.

[4] J.G. Leidenfrost, On the fixation of water in diverse fire, Int. J. Heat Mass Transf. 9 (1966) 1153–1166.

[5] K. Baumeister, F. Simon, Leidenfrost temperature - its correlation for liquid metals, cryogens, hydrocarbons, and water, J. Heat Transf. 95 (1973) 166–173.

[6] D. Quere, Leidenfrost dynamics, Annu. Rev. Fluid Mech. 45 (2013) 197–215.

[7] S.-J. Chen, A.A. Tseng, Spray and jet cooling in steel rolling, Int. J. Heat Fluid Flow 13 (1992) 358–369.

[8] A. Pola, M. Gelfi, G.L. Vecchia, Simulation and validation of spray quenching applied to heavy forgings, J. Mater. Process. Technol. 213 (2013) 2247–2253.

[9] S. Nižetic, D. Coko, A. Yadav, F. Grubišic-Cabo, Water spray cooling technique applied on a photovoltaic panel: the performance response, Energy Convers. Manage. 108 (2016) 287–296.

[10] S. Sargunanathan, A. Elango, S.T. Mohideen, Performance enhancement of solar photovoltaic cells using effective cooling methods: a review, Renew. Sustain. Energy Rev. 64 (2016) 382–393.

[11] G. Liang, I. Mudawar, Review of spray cooling – part 1: single-phase and nucleate boiling regimes, and critical heat flux, Int. J. Heat Mass Transf. 115 (2017) 1174–1205.

[12] G. Liang, I. Mudawar, Review of spray cooling – part 2: high temperature boiling regimes and quenching applications, Int. J. Heat Mass Transf. 115 (2017) 1206–1222.

[13] J. Breitenbach, I.V. Roisman, C. Tropea, From drop impact physics to spray cooling models: a critical review, Exp. Fluids 59 (2018) 55.

[14] J. Yang, L. Chow, M. Pais, Nucleate boiling heat transfer in spray cooling, J. Heat Transf. 118 (1996) 668–671.

[15] J. Kim, S. You, S.U. Choi, Evaporative spray cooling of plain and microporous coated surfaces, Int. J. Heat Mass Transf. 47 (2004) 3307–3315.

[16] K.A. Estes, I. Mudawar, Correlation of sauter mean diameter and critical heat flux for spray cooling of small surfaces, Int. J. Heat Mass Transf. 38 (1995) 2985–2996.

[17] J.D. Bernardin, I. Mudawar, Film boiling heat transfer of droplet streams and sprays, Int. J. Heat Mass Transf. 40 (1997) 2579–2593.

[18] L. Lin, R. Ponnappan, Heat transfer characteristics of spray cooling in a closed loop, Int. J. Heat Mass Transf. 46 (2003) 3737–3746.

[19] J. Breitenbach, I. Roisman, C. Tropea, Heat transfer in the film boiling regime: Single drop impact and spray cooling, Int. J. Heat Mass Transf. 110 (2017) 34–42.

[20] G. Liang, I. Mudawar, Review of drop impact on heated walls, Int. J. Heat Mass Transf. 106 (2017) 103–126.

[21] A.L. Yarin, I.V. Roisman, C. Tropea, Collision Phenomena in Liquids and Solids, Cambridge University Press, 2017.

[22] J. Bernardin, I. Mudawar, The Leidenfrost point: experimental study and assessment of existing models, J. Heat Transf. 121 (1999) 894–903.

[23] J. Bernardin, I. Mudawar, A cavity activation and bubble growth model of the Leidenfrost point, J. Heat Transf. 124 (2002) 864–874.

[24] J. Bernardin, I. Mudawar, A Leidenfrost point model for impinging droplets and sprays, J. Heat Transf. 126 (2004) 272–278.

[25] E. Aursand, S.H. Davis, T. Ytrehus, Thermocapillary instability as a mechanism for film boiling collapse, J. Fluid Mech. 852 (2018) 283–312.

[26] L. Xu, W.W. Zhang, S.R. Nagel, Drop splashing on a dry smooth surface, Phys. Rev. Lett. 94 (2005) 184505.

[27] S. Mandre, M. Mani, M.P. Brenner, Precursors to splashing of liquid droplets on a solid surface, Phys. Rev. Lett. 102 (2009) 134502.

[28] M. Mani, S. Mandre, M. Brenner, Events before droplet splashing on a solid surface, J. Fluid Mech. 647 (2010) 163–185.

[29] M.M. Driscoll, C.S. Stevens, S.R. Nagel, Thin film formation during splashing of viscous liquids, Phys. Rev. E 82 (2010) 036302.

[30] M. Driscoll, S. Nagel, Ultrafast interference imaging of air in splashing dynamics, Phys. Rev. Lett. 107 (2011) 154502.

[31] J. de Ruiter, J.M. Oh, D. van den Ende, F. Mugele, Dynamics of collapse of air films in drop impact, Phys. Rev. Lett. 108 (2012) 074505.

[32] J. de Ruiter, F. Mugele, D. van den Ende, Air cushioning in droplet impact. I. Dynamics of thin films studied by dual wavelength reflection interference microscopy, Phys. Fluids 27 (2015) 012104.

[33] J. de Ruiter, D. van den Ende, F. Mugele, Air cushioning in droplet impact. II. Experimental characterization of the air film evolution, Phys. Fluids 27 (2015) 012105.

[34] J. de Ruiter, R. Lagraaw, D. van den Ende, F. Mugele, Wettability-independent bouncing on flat surfaces mediated by thin air films, Nat. Phys. 11 (2015).

[35] E.Q. Li, S.T. Thoroddsen, Time-resolved imaging of a compressible air disc under a drop impacting on a solid surface, J. Fluid Mech. 780 (2015) 636–648.

[36] E.Q. Li, K.R. Langley, Y.S. Tian, P.D. Hicks, S.T. Thoroddsen, Double contact during drop impact on a solid under reduced air pressure, Phys. Rev. Lett. 119 (2017) 214502.

[37] F. Celestini, T. Frisch, Y. Pomeau, Room temperature water leidenfrost droplets, 2013. arXiv:1308.0941.

[38] D. Orejon, K. Sefiane, Y. Takata, Effect of ambient pressure on Leidenfrost temprerature, Phys. Rev. E 90 (2014) 053012.

[39] M.A.J. van Limbeek, P.B.J. Hoefnagels, M. Shirota, C. Sun, D. Lohse, Boiling regimes of impacting drops on a heated substrate under reduced pressure, Phys. Rev. Fluids 3 (2018) 053601.

[40] I. Buchmüller, Influence of pressure on Leidenfrost effect, Ph.D. thesis, Technische Universität Darmstadt, 2014.

[41] J. Breitenbach, I.V. Roisman, C. Tropea, Drop collision with a hot, dry solid substrate: Heat transfer during nucleate boiling, Phys. Rev. Fluids 2 (2017) 074301.

[42] J.R. Jaax, Orbiter integrated active thermal control subsystem test, NASA-CP-2150, 1980.

[43] R. Hatakenaka, J. Breitenbach, I.V. Roisman, C. Tropea, Y. Tagawa, Magic carpet breakup of a drop impacting onto a heated surface under reduced pressure, in: Proceedings of the 14th Triennial International Conference on Liquid Atomization and Spray Systems, 2018.

[44] X. Yu, R. Hu, X. Zhang, B. Xiea, X. Luo, Explosive bouncing on heated silicon surfaces under low ambient pressure, Soft Matter (2019).

[45] W. Tong, L. Qiu, J. Jin, L. Sun, F. Duan, Unique lift-off of droplet impact on high temperature nanotube surfaces, Appl. Phys. Lett. 111 (2017) 091605.

[46] M. Auliano, M. Fernandino, P. Zhang, C.A. Dorao, Water droplet impacting on overheated random si nanowires, Int. J. Heat Mass Transf. 124 (2018) 307–318.

[47] F. Moreau, P. Colinet, S. Dorbolo, Explosive Leidenfrost droplets, Phys. Rev. Fluids 4 (2019) 013602.

[48] V. Bertola, An impact regime map for water drops impacting on heated surfaces, Int. J. Heat Mass Transf. 85 (2015) 430–437.

[49] J.D. Bernardin, C.J. Stebbins, I. Mudawar, Mapping of impact and heat transfer regimes of water drops impinging on a polished surface, Int. J. Heat Mass Transf. 40 (1997) 247–267.

[50] R. Rioboo, C. Tropea, M. Marengo, Outcomes from a drop impact on solid surfaces, Atom. Sprays 11 (2001).

[51] H.J.J. Staat, T. Tran, B. Geerdink, G. Riboux, C. Sun, J.M. Gordillo, D. Lohse, Phase diagram for droplet impact on superheated surfaces, J. Fluid Mech. 779 (2015) R3.

[52] I.V. Roisman, J. Breitenbach, C. Tropea, Thermal atomisation of a liquid drop after impact onto a hot substrate, J. Fluid Mech. 842 (2018) 87–101.

[53] See Supplemental Material for videos of the outcomes of drop impact onto a heated substrate with moderate impact velocity as shown in Fig. 3, 2019.

[54] S. Nishio, K. Hirata, Study on the Leidenfrost temperature (1st report, experimental study on the fundamental characteristics of the Leidenfrost temperature), Trans. Japan Soc. Mech. Eng., Ser. B(in Japan.) 43 (1977) 3856–3867.

[55] C. Clanet, C. Beguin, D. Richard, et al., Maximal deformation of an impacting drop, J. Fluid Mech. 517 (2004) 199–208.

[56] S.J.D. van Stralen, R. Cole, W.M. Sluyter, M.S. Sohal, Bubble growth rates in nucleate boiling of water at subatmospheric pressures, Int. J. Heat Mass Transf. 18 (1975) 655–669.

[57] S. Chandra, C.T. Avedisian, On the collision of a droplet with a solid surface, Proc. Roy. Soc. Lond. Ser. A: Math. Phys. Sci. 432 (1991) 13–41.

[58] H. Chaves, A.M. Kubitzek, F. Obermeier, Dynamic processes occurring during the spreading of thin liquid films produced by drop impact on hot walls, Int. J. Heat Fluid Flow 20 (1999) 470–476.

[59] I. Roisman, E. Berberovic, C. Tropea, Inertia dominated drop collisions. I. On the universal flow in the lamella, Phys. Fluids 21 (2009).

[60] T. Ueda, Kieki Nisouryu - Nagare to Netsudentastu, Yokendo, 1981.

[61] S. Bankoff, Entrapment of gas in the spreading of a liquid over a rough surface, AIChE J. (1958) 24–26.

[62] V. Mehdi-Nejad, J. Mostaghimi, S. Chandra, Air bubble entrapment under an impacting droplet, Phys. Fluids 15 (2003) 173.

[63] S.T. Thoroddsen, T.G. Etoh, K. Takehara, N. Ootsuka, Y. Hatsuki, The air bubble entrapped under a drop impacting on a solid surface, J. Fluid Mech. 545 (2005) 203–212.

[64] W. Bouwhuis, R.C.A. van der Veen, T. Tran, et al., Maximal air bubble entrainment at liquid-drop impact, Phys. Rev. Lett. 109 (2012).

[65] M. Schremb, I.V. Roisman, C. Tropea, Transient effects in ice nucleation of a water drop impacting onto a cold substrate, Phys. Rev. E 95 (2017) 022805.

[66] B.B. Mikic, M. Rohsenow, Bubble growth rates in non-uniform temperature field, Adv. Heat Mass Transf. 2 (1969) 283–292.

[67] V.P. Carey, Liquid-Vapor Phase Change Phenomena, second ed., Hemisphere, New York, 1992.

[68] B.B. Mikic, M. Rohsenow, P. Griffith, On bubble growth rates, Int. J. Heat Mass Transf. 13 (1970) 657–666.

[69] Y.C. Lien, Bubble Growth Rates at Reduced pressure, Ph.D. thesis, Massachusetts Institute of Technology (1969).

[70] S.J.D. van Stralen, M.S. Sohal, R. Cole, W.M. Sluyter, Bubble growth rates in pure and binary systems: combined effect of relaxation and evaporation microlayers, Int. J. Heat Mass Transf. 18 (1975) 453–467.

[71] T.G. Theofanous, P.D. Patel, Universal relations for bubble growth, Int. J. Heat Mass Transf. 19 (1976) 425–429.

[72] A. Prosperetti, M.S. Plesset, Vapour-bubble growth in a superheated liquid, J. Fluid Mech. 85 (1978) 349–368.

[73] P. Stephan, J. Hammer, A new model for nucleate boiling heat transfer, Heat Mass Transf. 30 (1994) 119–125.

[74] C. Staszel, A. Yarin, Exponential vaporization fronts and critical heat flux in pool boiling, Int. Commun. Heat Mass Transf. 98 (2018) 171–176.

[75] H.T. Phan, N. Caney, P. Marty, S. Colasson, J. Gavillet, Surface wettability control by nanocoating: the effects on pool boiling heat transfer and nucleation mechanism, Int. J. Heat Mass Transf. 52 (2009) 5459–5471.

[76] H. Jo, H.S. Ahn, S. Kang, M.H. Kim, A study of nucleate boiling heat transfer on hydrophilic, hydrophobic and heterogeneous wetting surfaces, Int. J. Heat Mass Transf. 54 (2011) 5643–5652.

[77] R. Rioboo, M. Marengo, C. Tropea, Time evolution of liquid drop impact onto solid, dry surfaces, Exp. Fluids 33 (2002) 112–124.

[78] G. Riboux, J.M. Gordillo, Experiments of drops impacting a smooth solid surface: a model of the critical impact speed for drop splashing, Phys. Rev. Lett. 113 (2014) 024507.

[79] T.C. de Goede, K.G. de Bruin, N. Shahidzadeh, D. Bonn, Predicting the maximum spreading of a liquid drop impacting on a solid surface: effect of surface tension and entrapped air layer, Phys. Rev. Fluids 4 (2019) 053602.

[80] M.G. Cooper, A.J.P. Lloyd, The microlayer in nucleate pool boiling, Int. J. Heat Mass Transf. 12 (1969) 895–913.

[81] M. Cooper, The microlayer and bubble growth in nucleate pool boiling, Int. J. Heat Mass Transf. 12 (1969) 915–933.

[82] M. Shirota, M.A.J. van Limbeek, D. Lohse, C. Sun, Measuring thin films using quantitative frustrated total internal reflection (ftir), Eur. Phys. J. E 40 (2017).

[83] T. Yabuki, O. Nakabeppu, Heat transfer mechanisms in isolated bubble boiling of water observed with mems sensor, Int. J. Heat Mass Transf. 76 (2014) 286–297.